Modelling and
Simulation in Materials
Science and
Engineering

PAPER

Bridging length and time scales in predictive simulations of thermo-mechanical processes

To cite this article: Jiaqi Sun *et al* 2024 *Modelling Simul. Mater. Sci. Eng.* **32** 085015

IOP Publishing Modelling and Simulation in Materials Science and Engineering

Modelling Simul. Mater. Sci. Eng. **32** (2024) 085015 (20pp) https://doi.org/10.1088/1361-651X/ad89e4

Bridging length and time scales in predictive simulations of thermo-mechanical processes

Jiaqi Sun, Nicholas Taormina, Emir Bilgili, Yang Li and Youping Chen*

Department of Mechanical and Aerospace Engineering, University of Florida,
Gainesville, FL, United States of America

E-mail: ypchen2@ufl.edu

Received 19 June 2024; revised 7 October 2024
Accepted for publication 22 October 2024
Published 4 November 2024

Abstract

This work introduces a theoretical formulation and develops numerical methods for finite element implementation of the formulation so as to extend the concurrent atomistic-continuum (CAC) method for modeling and simulation of finite-temperature materials processes. With significantly reduced degrees of freedom, the CAC simulations are shown to reproduce the results of atomically resolved molecular dynamics simulations for phonon density of states, velocity distributions, equilibrium temperature field of the underlying atomistic model, and also the density, type, and structure of dislocations formed during the kinetic processes of heteroepitaxy. This work also demonstrates the need of a mesoscale tool for simulations of heteroepitaxy, as well as the unique advantage of the CAC method in simulation of the defect formation processes during heteroepitaxy.

Keywords: multiscale method, CAC, temperature, dislocations, epitaxy

1. Introduction

The microstructures of most technologically important materials involve multiple morphological length scales. These multiscale microstructures give rise to complex materials behaviors that are significantly different from those of perfect single crystals. As an example, polycrystalline ceramics typically consists of grains with size ranging from a few to hundreds of microns and grain boundaries (GBs) with thicknesses from a few angstroms to a few nanometers, as shown in figure 1 [1]. It is well known that polycrystalline materials are generally stronger and tougher than single crystals. GBs are responsible for the increased strength and toughness,

---

[*] Author to whom any correspondence should be addressed.

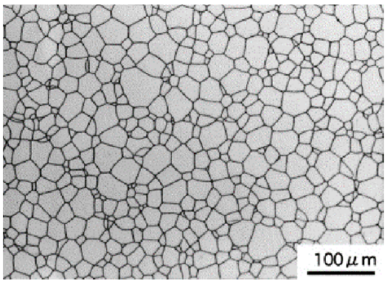

Figure 1. A reflection microscope photograph of YAG ceramics showing the micron-sized grains and nanometer-thick grain boundaries [1]. Reprinted from [1], Copyright (2002), with permission from Elsevier.

as they impede the motion of dislocations and cracks. To reproduce the physical processes underlying the improved strength and toughness, a simulation tool that explicitly resolves the multiple morphological scales is necessary.

Classical continuum theories have served as the major tool for the description and understanding of macroscopic material behavior [2]. However, classical theories cannot model multiscale microstructures without extensive experimental efforts or atomistic simulations to provide interfacial and microstructural properties. Atomically resolved methods, on the other hand, have difficulty in going beyond the nanoscale and hence are not tractable for the simulation of materials or structures with multiple morphological length scales. However, there is no need to model and simulate all ordered single crystal regions—such as a perfect single crystal grain in a polycrystalline material—with atomic resolution, as the distribution of the unit cells of a perfect crystal and the lattice displacements are continuous [3]. This has motivated the development of multiscale methods, with the aim to enable predictive simulation of materials and structures that have multiscale microstructures [4, 5].

There are two types of multiscale methods: sequential and concurrent. Sequential multiscale methods derive or fit parameters for a coarse-scale model from an underlying finer-scale model, such as from an electronic structure-based method to an atomistic model, or from an atomistic method to a continuum model. Concurrent multiscale methods, by contrast, concurrently couple two or more theoretical or materials descriptions in one model. Such methods may reduce degrees of freedom by only resolving disordered or critical regions such as the GBs or interphase boundaries with atomic resolution, while using a coarse-scale description for regions that exhibit continuous material behaviors. Most of early concurrent methods intuitively used the technique of domain decomposition that divides a material system into different domains, such as atomic and continuum regions [6–11], and describe the different domains using different theories and materials descriptions [12–16]. There are three-level concurrent multiscale methods.

(1) *Static or quasi-static methods* that solve time-independent or inertia-free problems. Most existing multiscale methods that are formulated based on force equilibrium and energy minimization belong to this category [17].
(2) *Dynamic methods* that simulate time-dependent processes underlying critical mechanical phenomena, the development of which was identified as a significant challenge in simulation-based engineering science by the computational science community [18, 19].

(3) *Coupled thermo-mechanical methods* that simulate dynamically coupled mechanical and thermal processes. There have been a few attempts to develop concurrent multiscale methods, in which the atomically resolved regions are governed by Newton's second law and the continuum or coarse-grained regions are governed by Fourier law of heat conduction [7, 8]. Success of such methods, however, has been limited.

Despite numerous theoretical or numerical methods for concurrent multiscale materials modeling and simulation have been proposed and published over the past decades, few of early concurrent multiscale methods were able to go beyond the nanoscopic length and time scale of the atomistic methods to simulate a system or a process of materials with microstructures at the mesoscale (100 nm to 100 μms). There were two common problems that have faced early multiscale methods:

(1) *Ghost forces*, a numerical artifact that is manifested as an unphysical force at or near the numerical interfaces due to the difference in governing equations for the same material. Ghost forces are present in almost all domain decomposition-based multiscale methods. The existence of ghost forces indicates a fundamental limitation of the methods for quantifying the properties of physical interfaces that link disparate length scales in materials with multiscale microstructures.
(2) *Spurious wave reflections*, manifested as reflected elastic waves by the numerical interfaces, due to different phonon/wave representations of the material by different theories. The spurious wave reflections unphysically increase the kinetic energy of fine-scale regions, leading to temperature rise and subsequently non-physical melting of the fine-scale regions, rendering most of domain decomposition-based multiscale methods powerless in dynamic simulations.

Both problems are caused by the difference in governing equations in early multiscale methods. In addition to different governing equations, another fundamental inconsistency is the difference in the definitions of basic physical quantities by different theoretical descriptions. For example, stress and heat flux in continuum theories are defined as a surface density [2, 20–24]; they are surface fluxes across real or imaginary surfaces [22]. By contrast, in most atomistic formulations and simulations, stress and heat flux are defined as a volume density [25–27]. Also, temperature in molecular kinetic theory and atomistic simulations is defined as a derived quantity in terms of the velocities of particles [28–30], whereas in continuum theories it is one of the basic quantities upon which all other quantities are defined [31, 32]. For coupled thermal mechanical problems, molecular simulations only solve the conservation equation of linear momentum, whereas continuum mechanics-based simulations must simultaneously solve both the conservation equations of linear momentum and energy. Moreover, a heat flux-temperature relationship must be prescribed in order for the energy equation to be solved for local temperature. The difference in temperature definition between molecular and continuum theories thus constitutes a fundamental challenge to the development of concurrent atomistic-continuum (CAC) methods for dynamically coupled thermal and mechanical problems.

The objective of this paper is to develop a Level-3 multiscale method that extends the CAC method to mesoscale simulation of coupled thermal mechanical problems. Following the introduction, section 2 reviews the theoretical formulation; section 3 develops a novel numerical method to implement the formulation and derives material parameters involved in the numerical implementation; section 4 demonstrates the efficacy of the numerical implementation, including comparisons of fully atomistic and CAC simulation results of phonon density of states (PDOSs), velocity distribution, and the distributions of kinetic energy (and hence temperature) and potential energy for various material systems; CAC simulation results of heteroepitaxial growth of PbTe on a PbSe (111) substrate, as well as the size effect of the substrate on dislocation density, are also presented in section 4. This paper concludes with a summary and discussions in section 5.

2. A review of CAC formulation and numerical implementation

The CAC methodology consists of a mathematical formulation and a modified finite element (FE) method to implement the formulation. The formulation extends Irving-Kirkwood's statistical mechanical theory for ensemble-averaged single-component single-phase hydrodynamical systems [33] to a CAC description that is valid for polyatomic crystalline materials at multiple length and time scales. It unifies not only atomistic and continuum representations of conservation laws but also the definitions of stress and heat flux [34–36]. The CAC formulation has been recently extended by redefining temperature as a derive quantity, thus unifying temperature definition in atomistic and continuum descriptions [37]. There are currently three published codes of the CAC methodology [38–40], and the codes have been tested through one-to-one comparisons with molecular dynamics (MD) simulations for multiscale problems, including crack initiation and branching [41, 42]; phase transitions [43]; dislocation nucleation and pattern formation [44–48], phonon-dislocation [49–51] and phonon-interface interactions [52, 53], etc.

The CAC formulation can also be viewed as a reformulation of continuum mechanics bottom up from the atomistics, which enables continuum mechanics to exactly represent the classical atomistic model, thereby expanding the scope, approach, and applicability of continuum mechanics, and naturally leading to a CAC methodology.

Different from classical continuum mechanics, the CAC formulation employs a two-level structural description, as shown in figure 2 [37], similar to that in Micromorphic theory [54–61]. By decomposing the position of an atom, $\boldsymbol{r}_{k\alpha}$, into the position of the lattice cell, $\boldsymbol{r}_k$, and the internal position of the atom relative to the lattice, $\Delta\boldsymbol{r}_{k\alpha}$, the local density of linear momentum (per unit cell volume) due to the αth atom can be expressed as

$$\begin{aligned}\rho_\alpha \boldsymbol{v}_\alpha &= \frac{1}{\Delta t}\int_t^{t+\Delta t} \mathrm{d}t \frac{1}{V}\iiint_V \mathrm{d}^3 r \sum_{k=1}^{N_l} m_\alpha \boldsymbol{v}_{k\alpha}\delta\left(\boldsymbol{r}-\boldsymbol{r}_{k\alpha}\right) \triangleq \sum_{k=1}^{N_l} m_\alpha \boldsymbol{v}_{k\alpha}\bar{\delta}_V\left(\boldsymbol{r}-\boldsymbol{r}_{k\alpha}\right)\\ &= \sum_{k=1}^{N_l}\sum_{\xi=1}^{N_a} m_\xi\, \boldsymbol{v}_{k\xi}\,\bar{\delta}_V\left(\boldsymbol{x}+\boldsymbol{y}-\boldsymbol{r}_k-\Delta\boldsymbol{r}_{k\alpha}\right),\end{aligned} \tag{1}$$

where N_l is the number of lattice cells in the system; δ is the delta distribution, or the Dirac delta defined by the sifting property [62], and $\boldsymbol{r} = \boldsymbol{x} + \boldsymbol{y}$, with $\boldsymbol{x}$ denoting the position of the unit cell and $\boldsymbol{y}$ the internal position relative to $\boldsymbol{x}$.

Multiplying both side of equation (1) by $\delta(\boldsymbol{y}-\Delta\boldsymbol{r}_{k\alpha})$and then integrating over the volume of ath atom, V_α, we obtain a different form of the local density of linear momentum:

$$\rho_\alpha \boldsymbol{v}_\alpha \equiv \sum_{k=1}^{N_l}\sum_{\xi=1}^{N_a} m_\xi\, \boldsymbol{v}_{k\xi}\,\bar{\delta}_V\left(\boldsymbol{x}-\boldsymbol{r}_k\right)\bar{\delta}_{V\alpha}\left(\boldsymbol{y}-\Delta\boldsymbol{r}_{k\alpha}\right), \tag{2}$$

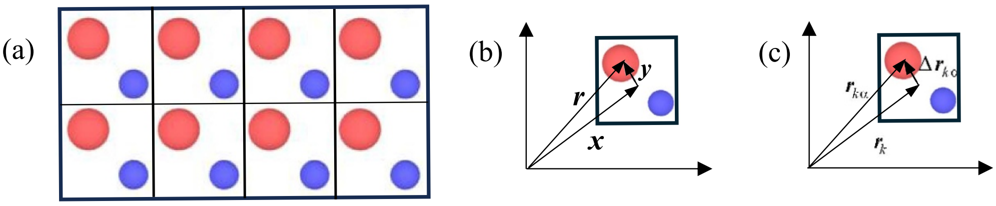

Figure 2. (a) Two-level structural description of crystal (replotted based on [3]), (b) field description of the position vector of a unit cell, $\boldsymbol{x}$, and the internal position of atom α relative to the unit cell, $\boldsymbol{y}$, (c) the corresponding positions in the phase space. Reproduced from [37], with permission from the Royal Society of Chemistry.

where N_a is the number of atoms within a lattice cell, V and V_α are the volume of the unit cell and of atom α within the unit cell, respectively, and the box functions are defined as

$$\bar{\delta}_V(\boldsymbol{x}-\boldsymbol{r}_k) = \frac{1}{\Delta t}\int_t^{t+\Delta t} \delta_V(\boldsymbol{x}-\boldsymbol{r}_k(\tau))\,\mathrm{d}\tau,\ \text{where}\delta_V(\boldsymbol{x}-\boldsymbol{r}_k) = \frac{1}{V}\begin{cases}1 \text{ if } \boldsymbol{x}-\boldsymbol{r}_k \in V\\ 0, \text{ if } \boldsymbol{x}-\boldsymbol{r}_k \notin V\end{cases}, \tag{3}$$

$$\begin{aligned}\bar{\delta}_{V\alpha}(\boldsymbol{y}-\Delta\boldsymbol{r}_{k\xi}) &= \frac{1}{\Delta t}\int_t^{t+\Delta t} \delta_{V\alpha}(\boldsymbol{y}-\Delta\boldsymbol{r}_{k\xi}(\tau))\,\mathrm{d}\tau,\ \text{where}\delta_{V\alpha}(\boldsymbol{y}-\Delta\boldsymbol{r}_{k\xi})\\ &= \begin{cases}1 & \text{if } \boldsymbol{y}-\Delta\boldsymbol{r}_{k\xi} \in V_\alpha \text{ or } \xi = \alpha\\ 0 & \text{if } \boldsymbol{y}-\Delta\boldsymbol{r}_{k\xi} \notin V_\alpha \text{ or } \xi \neq \alpha\end{cases},\end{aligned} \tag{4}$$

The time derivative of the linear momentum density defined in equation (2) can be obtained, using the theory of distributions [63, 64], as [33]

$$\frac{\partial(\rho_\alpha\boldsymbol{v}_\alpha)}{\partial t} = \frac{1}{V}\oiint_{\partial V}(\boldsymbol{t}_\alpha - \rho_\alpha\boldsymbol{v}_\alpha\boldsymbol{v}\cdot\boldsymbol{n})\,\mathrm{d}S + \frac{1}{V}\oiint_{\partial V_\alpha}(\boldsymbol{\tau}_\alpha - \rho_\alpha\boldsymbol{v}_\alpha\Delta\boldsymbol{v}_\alpha\cdot\boldsymbol{n})\,\mathrm{d}S_\alpha. \tag{5}$$

It is noticed that equation (5) is expressed in terms of two surface fluxes, $\boldsymbol{t}_\alpha$ and $\boldsymbol{\tau}_\alpha$, where $\boldsymbol{t}_\alpha$ is a momentum flux across the enclosing surface of a unit cell (the homogenous part of stress) and $\boldsymbol{\tau}_\alpha$ is the momentum flux across the enclosing surface of an atom within the unit cell (the inhomogeneous part of stress), with each further consisting a potential part due to the interaction forces between atoms and a kinetic part due to the motion of atoms. For explanation purposes, in equation (6), we present the obtained formula for the stress vector on a surface element at point $\boldsymbol{x}$ with normal $\boldsymbol{n}$ in a monatomic crystal. For detailed discussions of stress and heat flux polyatomic crystals, please see [36, 65–69],

$$\begin{aligned}\boldsymbol{t}(\boldsymbol{x},\boldsymbol{n}) &= \sum_{k,l(\neq k)}\frac{\partial\Phi_k}{\partial\boldsymbol{r}_l}\int_{L_{kl}}\bar{\delta}_A^n(\boldsymbol{\varphi}-\boldsymbol{x})\,\mathrm{d}\boldsymbol{\varphi} - \sum_k m_k\tilde{\boldsymbol{v}}_k\tilde{\boldsymbol{v}}_k\bar{\delta}_A^{\boldsymbol{n}}(\boldsymbol{x}-\boldsymbol{r}_k)\\ &= \sum_{k<l}\boldsymbol{F}_{kl}\int_{L_{kl}}\bar{\delta}_A^n(\boldsymbol{\varphi}-\boldsymbol{x})\,\mathrm{d}\boldsymbol{\varphi} - \sum_k m_k\tilde{\boldsymbol{v}}_k\tilde{\boldsymbol{v}}_k\bar{\delta}_A^{\boldsymbol{n}}(\boldsymbol{x}-\boldsymbol{r}_k),\end{aligned} \tag{6}$$

where Φ_k is the potential energy of atom k; $\boldsymbol{F}_{kl}$ is the interaction force between atom k and atom l, and $\bar{\delta}_A^n$ denotes an averaged Dirac delta over a surface element $\boldsymbol{A}$ and time step Δt. The first term in equation (6) represents the potential part of stress due to interaction forces across a surface element $\boldsymbol{A}$ that has area A and normal $\boldsymbol{n}$, with

$$\begin{aligned}\boldsymbol{F}_{kl}\int\limits_{\boldsymbol{L}_{kl}}\bar{\delta}_A^n\left(\boldsymbol{\varphi}-\boldsymbol{x}\right)\mathrm{d}\boldsymbol{\varphi} &\equiv \frac{1}{\Delta t}\int\limits_0^{\Delta t}\mathrm{d}\tau\frac{1}{A}\iint\limits_{\boldsymbol{A}}\int\limits_{\boldsymbol{L}_{kl}}\boldsymbol{F}_{kl}\delta\left(\boldsymbol{x}+\boldsymbol{x}'-\boldsymbol{\varphi}\right)\mathrm{d}\boldsymbol{\varphi}\cdot\boldsymbol{n}\mathrm{d}^2x' \\ &= \frac{\boldsymbol{F}_{kl}}{A}\begin{cases}1 \text{ if } \boldsymbol{r}_{kl}\text{intersects } \boldsymbol{A} \text{ and } \boldsymbol{n}\cdot\boldsymbol{L}_{kl}\geqslant 0 \text{ in } \Delta t\\ -1 \text{ if } \boldsymbol{r}_{kl}\text{intersects } \boldsymbol{A} \text{ and } \boldsymbol{n}\cdot\boldsymbol{L}_{kl}<0 \text{ in } \Delta t\\ 0 \text{ otherwise}\end{cases}. \end{aligned} \tag{7}$$

The second term represents the kinetic part of stress as a flow of momentum due to the thermal motion of atoms, with

$$\begin{aligned}m_k\tilde{\boldsymbol{v}}_k\tilde{\boldsymbol{v}}_k\bar{\delta}_A^{\boldsymbol{n}}\left(\boldsymbol{x}-\boldsymbol{r}_k\right) &\equiv \frac{1}{\Delta t}\int\limits_0^{\Delta t}\mathrm{d}\tau\frac{1}{A}\iint\limits_{\boldsymbol{A}}m_k\tilde{\boldsymbol{v}}_k\delta\left(\boldsymbol{x}-\boldsymbol{r}_k\right)\tilde{\boldsymbol{v}}_k\cdot\boldsymbol{n}\mathrm{d}\tau\mathrm{d}S \\ &= \frac{m_k\tilde{\boldsymbol{v}}_k}{A\Delta t}\begin{cases}1 \text{ if } \boldsymbol{r}_k\text{intersects } \boldsymbol{A} \text{ in } \Delta t \text{ and } \boldsymbol{n}\cdot\tilde{\boldsymbol{v}}_k\geqslant 0\\ -1 \text{ if } \boldsymbol{r}_k\text{intersects } \boldsymbol{A} \text{ in } \Delta t \text{ and } \boldsymbol{n}\cdot\tilde{\boldsymbol{v}}_k<0\\ 0 \text{ if } \boldsymbol{r}_{kl}\text{does not intersect } \boldsymbol{A}\end{cases}\end{aligned} \tag{8}$$

Alternatively, the distributional derivative of the linear momentum density can be derived from equation (1) [37] as

$$\rho_\alpha\dot{\boldsymbol{v}}_\alpha = \boldsymbol{f}^{\text{int}}\left(\boldsymbol{r},t\right)-\frac{1}{V}\oiint\limits_{\partial V}\sum_{k=1}^{N_l}m_\alpha\tilde{\boldsymbol{v}}_{k\alpha}\tilde{\boldsymbol{v}}_{k\alpha}\bar{\delta}\left(\boldsymbol{r}+\boldsymbol{r}'-\boldsymbol{r}_{k\alpha}\right)\cdot\boldsymbol{n}\mathrm{d}^2r' \triangleq \boldsymbol{f}^{\text{int}}\left(\boldsymbol{r},t\right)+\boldsymbol{f}^T\left(\boldsymbol{r},t\right) \tag{9}$$

where $\tilde{\boldsymbol{v}}_{k\alpha}\equiv\boldsymbol{v}_{k\alpha}-\boldsymbol{v}_\alpha$ is the difference between the particle velocity and the velocity field and $\boldsymbol{f}^T(\boldsymbol{r},t)$ is related to thermal fluctuations or the kinetic part of stress.

Note that temperature is a statistically averaged quantity related to kinetic energy and that the kinetic energy density due to α-species can be decomposed into two parts: one due to the velocity field and one due to difference between particle velocity and the velocity field, i.e.

$$\begin{aligned}\left\langle\sum_{k=1}^{N_l}\frac{1}{2}m_\alpha\left(\boldsymbol{v}_{k\alpha}\right)^2\delta_V\left(\boldsymbol{r}-\boldsymbol{r}_{k\alpha}\right)\right\rangle &= \frac{1}{2}\rho_\alpha\left(\boldsymbol{v}_\alpha\right)^2+\left\langle\iiint\limits_V\sum_{k=1}^{N_l}\frac{1}{2}m_\alpha\left(\tilde{\boldsymbol{v}}_{k\alpha}\right)^2\delta_V\left(\boldsymbol{r}-\boldsymbol{r}_{k\alpha}\right)\right\rangle \\ &\equiv \left\langle k_{\alpha 1}\left(\boldsymbol{r},t\right)\right\rangle+\left\langle k_{\alpha 2}\left(\boldsymbol{r},t\right)\right\rangle = \frac{3}{2}k_{\mathrm{B}}T\left(\boldsymbol{r},t\right),\end{aligned} \tag{10}$$

where k_{a1} is the density of the kinetic energy due to velocity field, which can be described by the motion of FEs, and k_{a2} is the density of the kinetic energy of phonons that are cut off by the FE linear shape functions.

The ensemble averaged equation (9) can then be expressed in terms of temperature as

$$\left\langle\rho_\alpha\dot{\boldsymbol{v}}_\alpha\right\rangle = \left\langle\boldsymbol{f}^{\text{int}}\right\rangle+\left\langle\boldsymbol{f}^T\right\rangle = \left\langle\boldsymbol{f}^{\text{int}}\right\rangle-\beta\nabla T. \tag{11}$$

Equation (11) is a statistically averaged linear momentum equation. It is expressed in terms of temperature field and hence represents Newton's second law only in statistical sense, as$\boldsymbol{f}^T(\boldsymbol{r},t)$ is a fluctuating function of time at finite temperature. In a previous work, we showed that this fluctuating force cannot be simply expressed as a Markov random force, but a combination of a random force and a frictional or damping force. Consequently, the instantaneous form of equation (11), i.e. equation (9), can be expressed, in the form of the generalized Langevin equation [70, 71], as

$$\rho_\alpha \dot{\boldsymbol{v}}_\alpha = \boldsymbol{f}^{\text{int}}(\boldsymbol{r},t) - \beta\left[\nabla T + \boldsymbol{\eta}(t) + \int_{t-T_\text{c}}^{t} \gamma(t-\tau)\boldsymbol{v}_\alpha(\boldsymbol{r},\tau)\,\text{d}\tau\right], \tag{12}$$

where $\boldsymbol{\eta}(t)$ is a time-correlated Gaussian random process and γ a dissipative memory kernel and is related to $\boldsymbol{\eta}(t)$, i.e.

$$\langle\boldsymbol{\eta}(t)\rangle = 0,\ \langle\eta_i(t)\eta_j(\tau)\rangle = \delta_{ij}C(t-\tau),\ \text{and}\ C(t-\tau) = \frac{2g}{\sigma\sqrt{2\pi}}\exp\left(-\frac{(t-\tau)^2}{2\sigma^2}\right), \tag{13}$$

and

$$\gamma(t-\tau) = \frac{1}{k_\text{B}T}C(t-\tau), \tag{14}$$

where σ is the standard deviation of the Gaussian distribution, *2* g is the strength of $\boldsymbol{\eta}(t)$, and T_c is the longest period of the vibration mode that is cut off by FE shape functions.

3. Numerical implementation

It is noticed from equation (12) that the fluctuating force $\boldsymbol{\eta}(t)$ enters the linear momentum equation when there are short-wavelength phonons being cut off by FE shape functions. Thus, it can be generated using the trigonometric representation of Gaussian processes in terms of the frequencies of the missing phonons, i.e.,

$$\eta_i(t) = \sum_{m=1}^{N_\text{c}}\left[A_m\sin\omega(k_m)t + B_m\cos\omega(k_m)t\right] = \sum_{m=1}^{N_\text{c}}A_m\sin(\omega_m t + \phi_m), \tag{15}$$

where N_c is the total number of omitted phonons in each element; $\omega(k_m)$ is the frequency of the omitted phonons with wavevector k_m, which can be determined from the phonon dispersion relations. A_m is the amplitude of the fluctuation force associated with phonon mode m, ϕ_m is the phase and can be random. Assuming the mass density is constant within each element, we can obtain the velocity response to the fluctuation force as

$$\rho v_i = -\sum_{m=1}^{N_\text{c}}\frac{A_m}{\omega_m}\cos(\omega_m t + \phi_m). \tag{16}$$

At thermal equilibrium, each degree of freedom has the same averaged kinetic energy density $k_\text{B}T/2V$, where $V = m/\rho$ is the volume of the primitive unit cell at point $\boldsymbol{x}$. We thus obtain the amplitude A_m as

$$A_m = \frac{\omega_m}{V}\sqrt{\frac{2mk_\text{B}T}{N_\text{c}}}. \tag{17}$$

Approximating the displacement field of αth atom in an element V_e as $\boldsymbol{u}_\alpha(\boldsymbol{x}) = \Phi_\eta(\boldsymbol{x})\boldsymbol{U}_{\eta\alpha}$, where $\Phi_\eta(\boldsymbol{x})$ is the shape functions, the weak form of equation (12) is then expressed as

$$\left(\iiint\limits_{V_\mathrm{e}} \rho_\alpha \Phi_\xi \Phi_\eta \mathrm{d}V\right)\ddot{\boldsymbol{U}}_{\eta\alpha} + \left(\iiint\limits_{V_\mathrm{e}} \rho_\alpha \Phi_\xi \Phi_\eta \mathrm{d}V \int\limits_{t-T_\mathrm{c}}^{t} \gamma(t-\tau)\dot{\boldsymbol{U}}_{\eta\alpha}(\tau)\,\mathrm{d}\tau\right)$$
$$= \iiint\limits_{V_\mathrm{e}} \Phi_\xi \boldsymbol{f}_\alpha^{\mathrm{int}} \mathrm{d}V - \iiint\limits_{V_e} \Phi_\xi\left(\beta\nabla T - \boldsymbol{\eta}(t)\right)\mathrm{d}V. \tag{18}$$

Equation (18) is a general FE equation. The integrals can be numerically evaluated using Gaussian quadrature. Note that the temperature gradient is zero for systems at thermal equilibrium and a constant for steady-state systems. Thus, $\beta\nabla T - \boldsymbol{\eta}(t)$ does not vary in space, i.e. is only a function of time, within a FE, if the conventional tri-linear shape functions are employed for the FEs. Thus, no numerical integration is needed for the last integral.

To summarize, the numerical implementation involves the following variables:

1. β is a constant parameter to be determined by the resolution of a measurement. For a system discretized by 8-node hexahedral elements and each element contains n_l unit cells, the ratio of the DOFs of the FEs and that of a corresponding atomically resolved model is $8/n_l$. The equipartition theorem then gives $\beta = 3(n_l - 8)k_\mathrm{B}/V_\mathrm{e}$.
2. $\omega(k_m)$, is the frequency of the omitted phonons with wavevector k_m, which can be determined from the frequency–wavevector relations, i.e., phonon dispersion relations.
3. A_m, the amplitude of the fluctuating force associated with phonon mode m, which is related to temperature.
4. ϕ_m, the phase of each sine function, which can be random.
5. T_c is the time interval in the dissipative memory kernel and can be selected to be $2\pi/\omega$, where ω is the lowest frequency of the missing phonons for a FE. T_c can be selected as the longest period among the N_c vibration modes that are cut off by the FE shape functions,
6. N_C, the total number of omitted phonons in an element, which can also be determined from phonon dispersion relation. For more discussions of N_C, please see [72].

4. Numerical examples

4.1. Verifications

In classical mechanics of particles, temperature is defined in terms of particle velocities, or more precisely, the kinetic energy of particles, using molecular kinetic theory. The quantum description of temperature, however, is expressed in terms of phonons. A phonon is a collective excitation or motion of atoms at a specific frequency and polarization. There are more phonons at high temperatures and fewer phonons at low temperatures. The PDOSs is defined as $g(\omega)$ such that the number of phonon modes with angular frequencies between ω and $\omega + \mathrm{d}\omega$ is equal to $g(\omega)\,\mathrm{d}\omega$ [73]. It is the measure of phonon distribution in a material and can be computed as the power spectrum of the mass-weighted velocity correlation function.

To quantify the accuracy and efficiency of the numerical implementation of the formulation, we created four CAC models of thermally equilibrated single crystals Fe, Si, PbTe, and PbSe, respectively, as well as the corresponding all-atom models. We employ the EAM interatomic

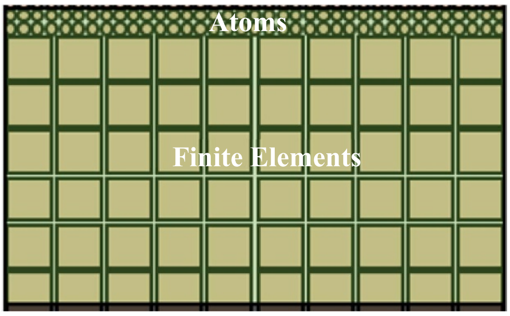

Figure 3. Schematic of a CAC model that consists of both atoms and finite elements.

Table 1. Details of the computer models.

Material system	Fe	Si	PbSe	PbTe
Number of atoms in the atomically resolved region	512 000	442 368	307 200	307 200
Number of elements in the FE region	16 000	3456	7200	7200
Number of atoms in the corresponding all atom model	16 896 000	14 598 144	7680 000	7680 000

potential for Fe [74], the Stillinger–Weber potential for Si [75], and the Buckingham–Coulombic interatomic potential for PbTe and PbSe [76, 77] to describe the atomic interactions in each system. The dimension of each model is about 50 nm × 50 nm × 100 nm, in which the ratio of the volume for the atomically resolved region and that for the FE region is 1:32. All CAC models are discretized with a uniform mesh and an atomically resolved region, as shown in figure 3. Other details of the computer models are summarized in table 1, including the number of atoms, the number of elements, and the equivalent total number of atoms.

In figure 4, we compare the PDOSs computed by CAC with that by MD for the four systems at 300 K, respectively. It is seen from figure 4 that the PDOS for the four systems computed by CAC are in excellent agreement with those obtained by MD, indicating that all the phonons that are present in the atomically resolved MD simulations have been fully captured by the CAC simulations with a significantly reduced degrees of freedom.

To test how well the CAC FE representation in reproducing the temperature field of the underlying atomistic model, we have simulated four systems that are thermally equilibrated at temperature 300 K. In figure 5, we plot the kinetic energy and potential energy distributions in the Si and PbSe models, respectively. As can be seen from figure 5, the difference in the kinetic energy density reproduced by MD and that by the CAC FEs is 6.7% and 7.7% for the two models, respectively. This demonstrates that CAC FEs can reproduce the temperature field of their underlying atomically resolved models. The results also show that we can use a small atomic region to serve as a heat bath for finite-temperature CAC simulation, as shown in figure 3.

The above simulations solve the instantaneous conservation equation of linear momentum equation (12), which is an approximate form of equation (9) at the atomic scale and satisfies

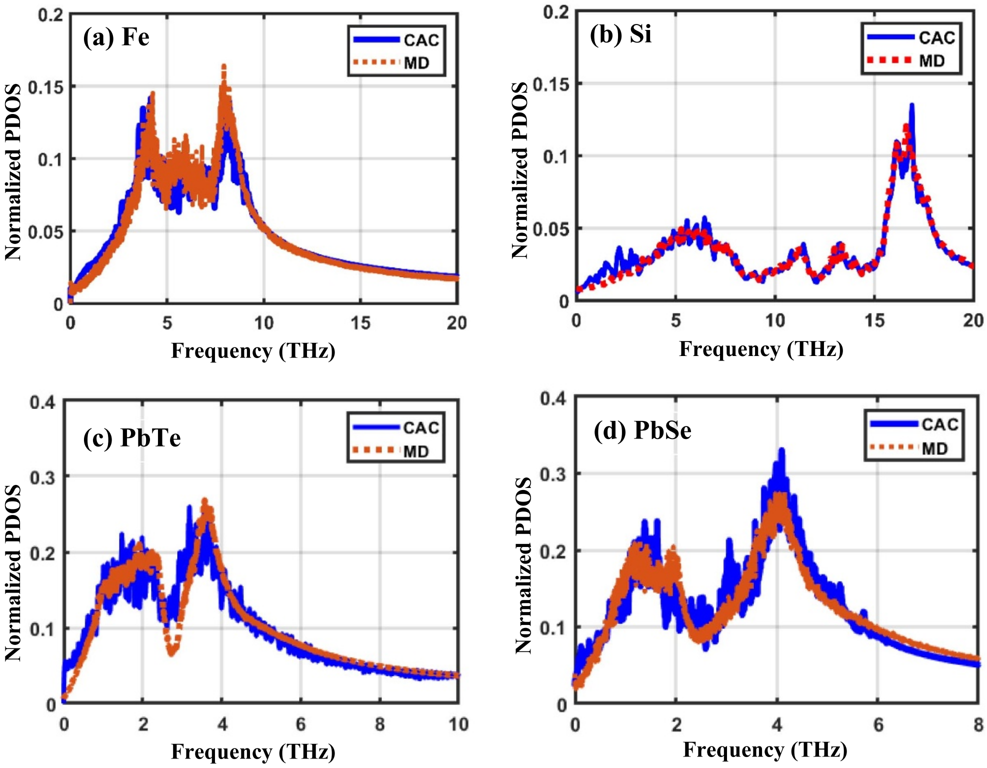

Figure 4. Comparisons of MD and CAC simulation results of normalized phonon density of state (PDOS) for (a) Fe, (b) Si, (c) PbTe, and (d) PbSe. Each finite element in the CAC models contains 512 primitive unit cells. All the PDOS are computed from the Fourier transform of the velocity autocorrelation functions at 300 K.

the statistically averaged equation of motion, equation (11). Note that equation (9) and (11) represent the linear momentum equation at two different time scales, with the former being derived as a direct consequence of Newton's equation of motion and holds at atomic length and time in the sense of distributions, while the latter holds only statistically or at larger time scales. Thus, there is an alternative approach, method 2, to simulate the computer model in figure 3 by using equation (11) for the FE region, while equation (9) for the atomically resolved region. In figure 6, we compare the velocity distribution of the atomic region in the CAC model with that in an atomically resolved region at 300 K. As can be seen from figure 6, there is an excellent agreement between the velocity distributions of the atoms in the two different simulations and both obey the Maxwell–Boltzmann distribution. These numerical examples further demonstrate the accuracy and efficiency of the formulation and the numerical methods in simulations of finite-temperature problems.

4.2. *Multiscale simulation of molecular beam epitaxy*

Heteroepitaxy is a widely used bottom–up method in the manufacture of semiconductor devices [78]. Regardless of the growth mechanisms, increasing epilayer thickness will unavoidably lead to misfit dislocation generation and concomitant threading dislocations [79,

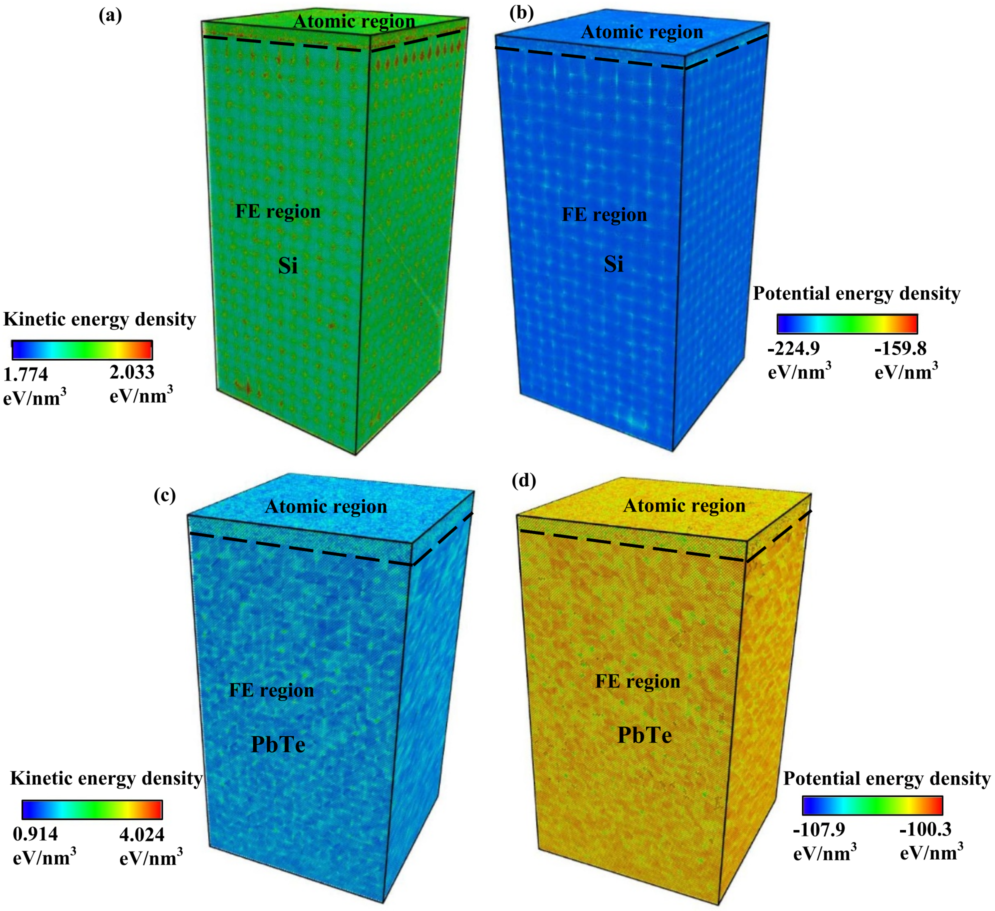

Figure 5. (a) Distributions of the kinetic energy density and (b) potential energy density in the CAC model of Si; distributions of the (c) kinetic energy density and (d) potential energy density in the CAC model of PbTe. The unit in the color bar is eV nm^{-3}. Dash lines indicate an interface between the coarse-scale FE region and atomic region.

80]. The structure and density of the dislocations are experimentally found to depend on growth temperature [79–83] and also the size of the substrate [84, 85]. Predicting the dislocation structure and density in heteroepitaxial growth thus requires a predictive mesoscale method. The advantage for CAC for simulation of heteroepitaxial processes is that the meso or macro-scale substrates can be modeled using coarse-scale FEs, as shown in figure 7, while the growth process is simulated with atomic resolution.

In order to compare the CAC simulation results of the kinetic processes of molecular beam epitaxy with that by MD, we constructed a small computer model for simulation of epitaxial growth of PbTe on a PbSe (111) substrate with dimensions of 50 nm × 50 nm × 10 nm. This is the size that can be simulated by both MD and CAC. The substrate in the CAC model is discretized into coarse-scale FEs; only the top surface of the substrate is modeled in terms of atoms. All the FEs have the rhombohedral shape with each node containing a primitive unit cell of the PbSe crystal.

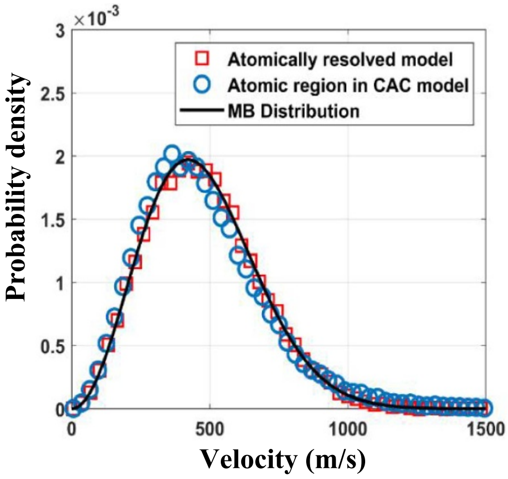

Figure 6. Velocity distribution of Si atoms in the atomic region of the CAC model (blue circle) and that in the atomically resolved model (red square). The black line represents the Maxwell–Boltzmann distribution of Si atoms at 300 K.

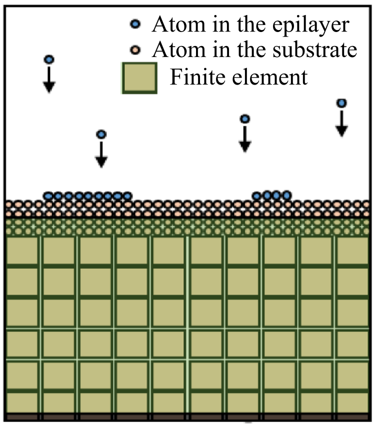

Figure 7. Schematic of a CAC model of heteroepitaxial growth, in which the substrate is modeled with finite elements, with the top layers of the substrate and the epitaxial process being modeled with atomic resolution.

In figure 8, we compare the CAC and MD simulation results of the atomic position of the epilayer, as well as the dislocation structure. As can be seen from figures 8(a) and (b), the CAC simulation results of the dislocation network agree well with those obtained by MD. This excellent agreement demonstrates that, with significantly reduced DOFs, CAC can reproduce the kinetic processes of the formation of dislocations in PbTe on PbSe (111) heteroepitaxial systems in excellent agreement with that by MD.

To demonstrate the effect of the substrate size, we have simulated the epitaxial growth of PbTe on PbSe (111) substrate with area of 50 × 50 nm, but two different thicknesses (10 nm and 100 nm, respectively). Figure 9 compares the dislocation density and dislocation networks

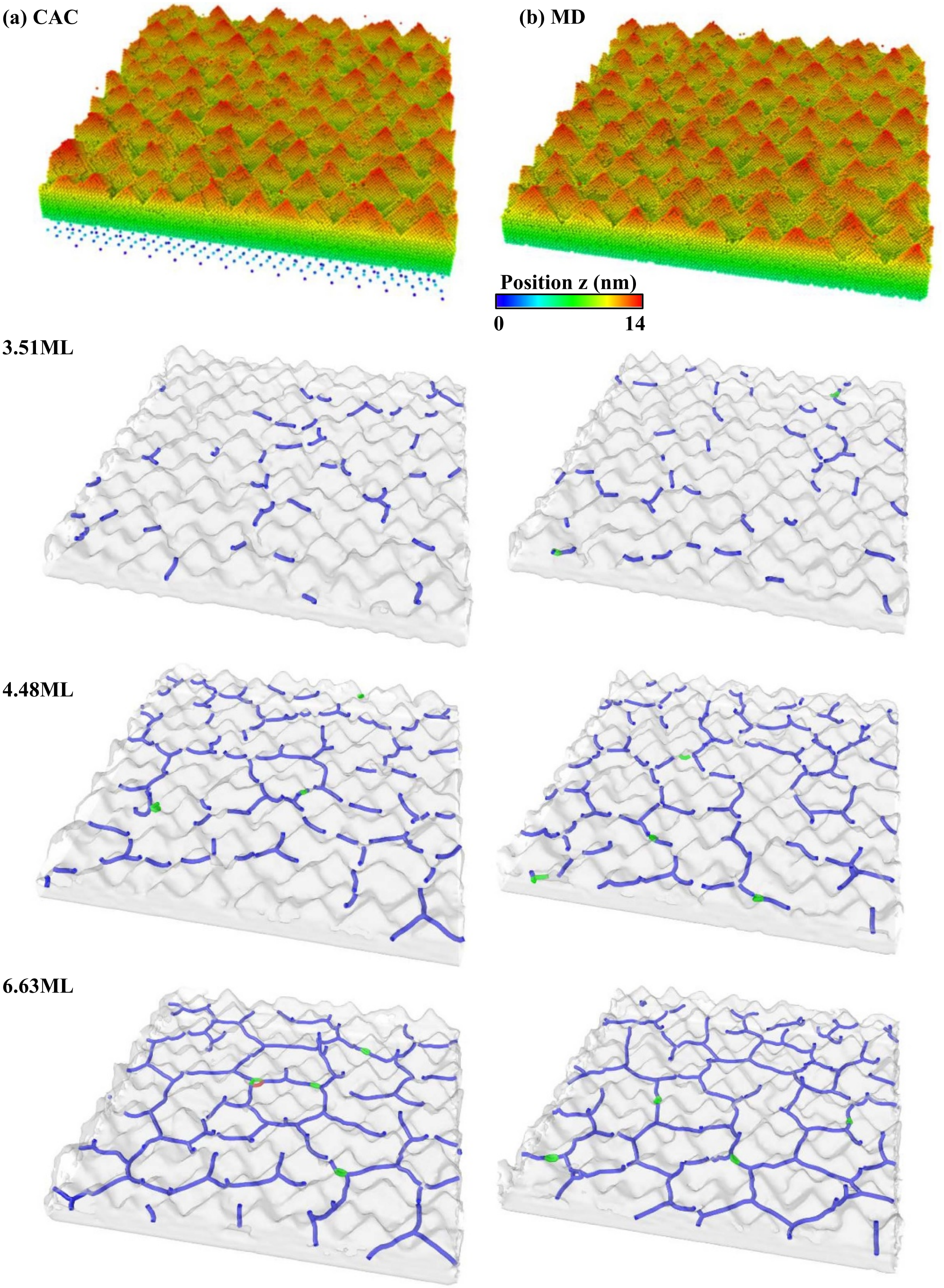

Figure 8. A comparison between (a) CAC and (b) MD simulation results of atomic position and dislocation networks in an PbTe/PbSe (111) epitaxial structure as a function of epilayer coverages. The dislocations are visualized using OVITO DXA (Dislocation Extraction Algorithm) [86].

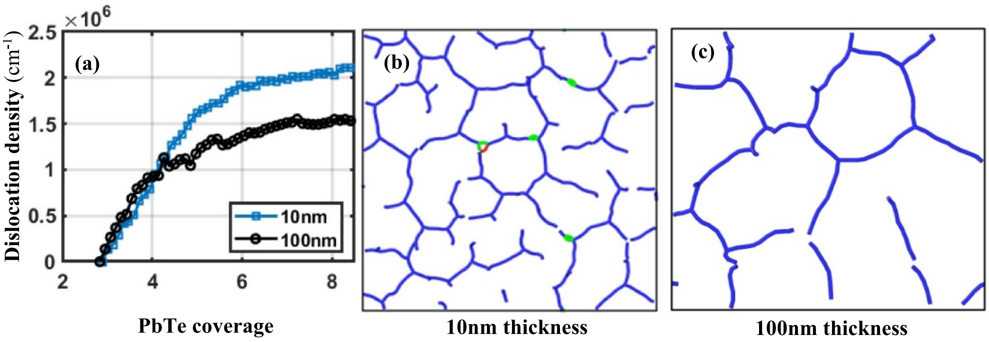

Figure 9. (a) Dislocation density per interface area as a function of PbTe layer thickness during the growth of PbTe on PbSe (111) substrates. PbSe substrates have surface areas of 50 × 50 nm^2 and substate thicknesses of 10 nm or 100 nm. Dislocation networks in the interface resulting from the growth of PbTe on PbSe substrates with (b) 10 nm thickness and (c) 100 nm thickness.

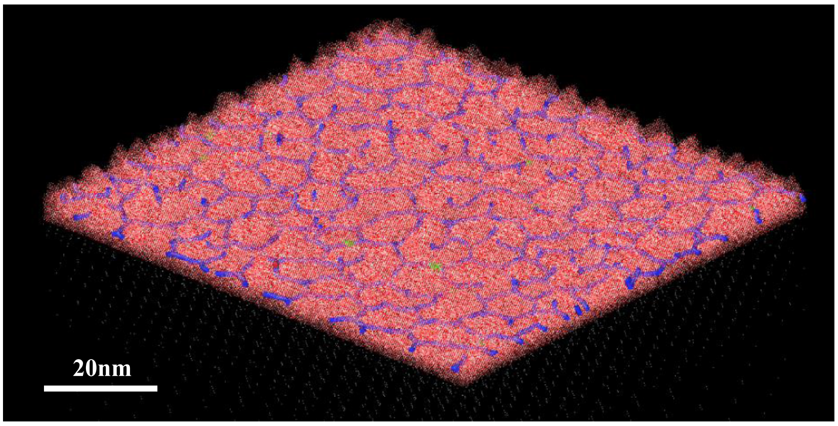

Figure 10. Perspective view of the dislocation network at PbTe/PbSe (111) interface at 6.3 ML PbTe coverage, grown on a PbSe (111) substrate with dimensions of 100 nm × 100 nm × 100 nm, obtained via CAC simulation, visualized using DXA [86] in OVITO.

for the two different substrate sizes. It is seen from figure 9, a difference in substrate size leads not only to different dislocation densities but also different dislocation structures and types.

To further demonstrate the CAC method for mesoscale simulation of molecular beam epitaxy, the growth process of PbTe on a PbSe (111) substrate that has dimensions of 100 nm × 100 nm × 100 nm is simulated with a growth temperature of 650 K, as that in the PbTe/PbSe epitaxial experiment by Springholz, G. and Wiesauer [87]. In figure 10, we present a perspective view of the dislocation network formed during the epitaxial growth at the epilayer thickness of 6.3 monolayers (ML). In figures 11 and 12, we present two zoomed-in side views of the threading dislocations.

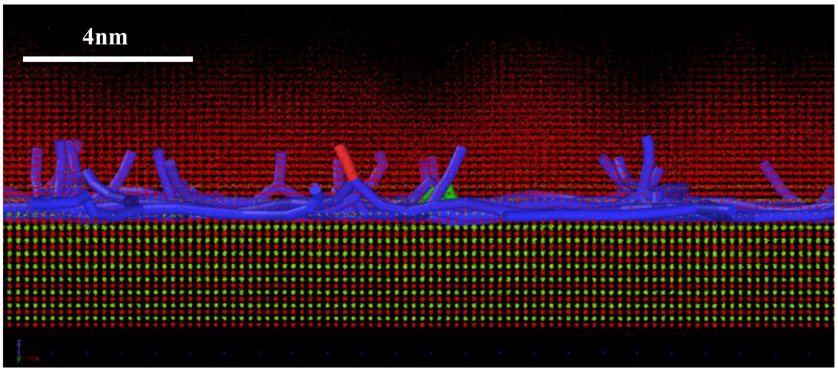

Figure 11. Zoomed-in side view of the PbTe/PbSe (111) interface at 6.3 ML PbTe coverage, obtained by CAC simulation of PbTe/PbSe heteroepitaxy with substrate dimensions of 100 nm × 100 nm × 100 nm, showing the threading dislocations, visualized using OVITO DXA [86]. Blue lines represent $1/2$ <110> dislocations, green lines represent 1/6 <112> Shockley dislocations and red lines represent other dislocation types.

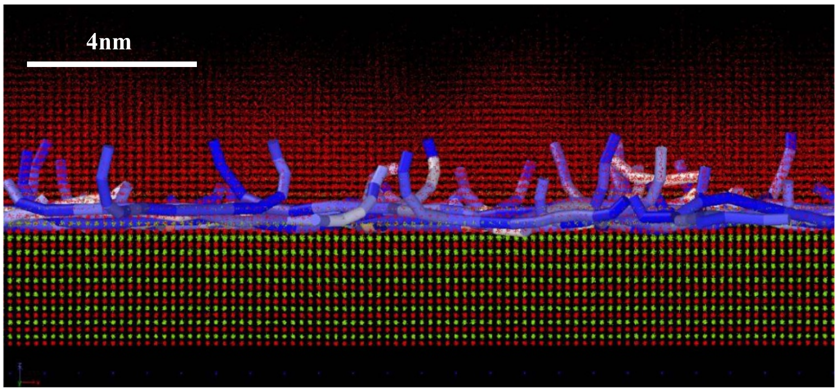

Figure 12. Zoomed-in side view of the PbTe/PbSe (111) interface at 6.3 ML PbTe coverage, obtained by CAC simulation of PbTe/PbSe heteroepitaxy with substrate dimensions of 100 nm × 100 nm × 100 nm, showing the threading dislocations, visualized using OVITO DXA [86]. Blue lines represent $1/2$ <110>(001) dislocations. Red lines represent $1/2$ <110>{111} dislocations.

5. Summary

In this work, we have discussed and analyzed the current state of concurrent multiscale methods. We have then reviewed the theoretical formulation of the CAC method for simulation of materials processes at finite temperature, developed numerical methods, and derived all parameters involved in the numerical implementation. By defining temperature as a derived quantity and rederiving the balance equation of linear momentum, the CAC method has been shown to reproduce the PDOSs of Si, Fe, PbTe, and PbSe single crystals, in excellent agreement with atomically resolved MD simulation results. Using about 1.56% of the degrees of freedom of the underlying atomistic models, these FEs have reproduced the spatial distributions of the potential energy density as well as the kinetic energy density, and hence the temperature field, of the underlying atomistic models. It is also noticed that there is no appreciable discontinuity at the atomic-FE interface for kinetic and potential energy distributions. In addition, CAC simulation results of PbTe/PbSe (111) heteroepitaxy are shown to compare very well with atomically-resolved MD simulation results, including the structure, type, and density of dislocations formed during heteroepitaxial processes of PbTe growth on PbSe (111). The applicability and the unique advantage of the CAC method for mesoscale simulation of epitaxial processes, which are high-temperature highly nonequilibrium processes, to predict the formation of misfit and threading dislocation networks during heteroepitaxy are clearly demonstrated. In addition, the effects of substrate size further justify the need to mesoscale or macroscale simulations in order to study heteroepitaxy and predict dislocation formation during epitaxial processes.

We would like to note that this work is mainly focused on the FE implementation of the CAC formulation. The effect of thermal fluctuations by short wavelength phonons in the FE representation is derived based on the consideration of local thermal equilibrium. Further theoretical and numerical research will be needed to fully address the length and time scale challenge in modeling and simulation of multiscale structured materials or highly nonequilibrium processes such as thermally activated dislocations [88–90] and phonon thermal transport [91, 92].

Data availability statement

All data that support the findings of this study are included within the article (and any supplementary files).

Acknowledgment

This work is based on research supported by the US National Science Foundation under Award Number CMMI-2054607. The work of Emir Bilgili is supported by the US National Science Foundation under Award Number DMR 2121895. The computer simulations are funded by the Advanced Cyberinfrastructure Coordination Ecosystem: Services & Support (ACCESS) allocation TG-DMR190008.

ORCID iDs

Jiaqi Sun https://orcid.org/0000-0003-2570-7718
Nicholas Taormina https://orcid.org/0009-0000-5961-8516
Emir Bilgili https://orcid.org/0009-0002-7531-7996
Yang Li https://orcid.org/0000-0003-1171-0852
Youping Chen https://orcid.org/0000-0002-9626-9009

References

[1] Ikesue A 2002 Polycrystalline Nd: YAG ceramics lasers *Opt. Mater.* **19** 183–7
[2] Eringen A C 1980 Mechanics of continua *rek*
[3] Kittel C 2005 *Introduction to Solid State Physics* (Wiley)
[4] Hemminger J, Crabtree G and Sarrao J 2012 From quanta to the continuum: opportunities for Mesoscale Science *A Report from the Basic Energy Sciences Advisory Committee, Technical Report* pp 1601–6

[5] Dolbow J, Khaleel M and Mitchell J 2004 Multiscale mathematics initiative: a roadmap *US Department of Energy, Report No. PNNL-14966*

[6] Moseley P, Oswald J and Belytschko T 2012 Adaptive atomistic-to-continuum modeling of propagating defects *Int. J. Numer. Methods Eng.* **92** 835–56

[7] Jeremy A T, Reese E J and Gregory J W 2010 Application of a field-based method to spatially varying thermal transport problems in molecular dynamics *Modelling Simul. Mat. Sci. Eng.* **18** 085007

[8] Wagner G J, Jones R E, Templeton J A and Parks M L 2008 An atomistic-to-continuum coupling method for heat transfer in solids *Comput. Methods Appl. Mech. Eng.* **197** 3351–65

[9] Davis A S, Lloyd J T and Agrawal V 2022 Moving window techniques to model shock wave propagation using the concurrent atomistic–continuum method *Comput. Methods Appl. Mech. Eng.* **389** 114360

[10] Eidel B and Stukowski A 2009 A variational formulation of the quasicontinuum method based on energy sampling in clusters *J. Mech. Phys. Solids* **57** 87–108

[11] Davis A S and Agrawal V 2023 Investigating shock wave propagation, evolution, and anisotropy using a moving window concurrent atomistic–continuum framework *Comput. Mech.* **71** 721–43

[12] Rudd R E and Broughton J Q 2005 Coarse-grained molecular dynamics: nonlinear finite elements and finite temperature *Phys. Rev.* B **72** 144104

[13] Rudd R E 2005 Concurrent multiscale simulation at finite temperature: coarse-grained molecular dynamics *Handbook of Materials Modeling* (Springer) pp 649–61

[14] Dewald M and Curtin W A 2011 Multiscale modeling of dislocation/grain-boundary interactions: III. 60° dislocations impinging on $\Sigma3$, $\Sigma9$ and $\Sigma11$ tilt boundaries in Al *Modelling Simul. Mat. Sci. Eng.* **19** 055002

[15] Dewald M and Curtin W A 2006 Analysis and minimization of dislocation interactions with atomistic/continuum interfaces *Modelling Simul. Mat. Sci. Eng.* **14** 497

[16] Dewald M P and Curtin W A 2007 Multiscale modelling of dislocation/grain-boundary interactions: i. Edge dislocations impinging on $\Sigma11$ (1 1 3) tilt boundary in Al *Modelling Simul. Mat. Sci. Eng.* **15** S193

[17] Chen Y, Zimmerman J, Krivtsov A and McDowell D L 2011 Assessment of atomistic coarse-graining methods *Int. J. Eng. Sci.* **49** 1337–49

[18] Glotzer S C, Kim S, Cummings P T, Deshmukh A, Head-Gordon M, Karniadakis G, Petzold L, Sagui C and Shinozuka M 2009 International assessment of research and development in simulation-based engineering and science *Panel report; World Technology Evaluation Center Inc Baltimore MD* (https://doi.org/10.1021/nl9000794)

[19] Oden J, Belytschko T, Fish J, Hughes T, Johnson C, Keyes D, Laub A, Petzold L, Srolovitz D and Yip S 2006 Simulation-based engineering science: revolutionizing engineering science through simulation *Report of the National Science Foundation Blue Ribbon Panel on Simulation-Based Engineering Science. Tech. Rep.* 65

[20] Miller G A 1909 Proposed publication of Euler's works *Science* **30** 10–12

[21] Truesdell C A 1992 Cauchy and the modern mechanics of continua *Revue d'histoire Des. Sci.* **45** 5–24

[22] Cauchy A L B 1823 *Recherches sur l'équilibre et le mouvement intérieur des corps solides ou fluides, élastiques ou non élastiques*

[23] Truesdell C and Noll W 2004 The non-linear field theories of mechanics *The Non-linear Field Theories of Mechanics* (Springer) pp 1–579

[24] Truesdell C A 1992 *A First Course in Rational Continuum Mechanics V1* (Academic)

[25] Lehoucq R B and Von Lilienfeld-Toal A 2010 Translation of Walter Noll's "Derivation of the fundamental equations of continuum thermodynamics from statistical mechanics" *J. Elast.* **100** 5–24

[26] Hardy R J 1982 Formulas for determining local properties in molecular-dynamics simulations: shock waves *J. Chem. Phys.* **76** 622–8

[27] Allen P B and Feldman J L 1993 Thermal conductivity of disordered harmonic solids *Phys. Rev.* B **48** 12581

[28] Clausius R XI. 1857 On the nature of the motion which we call heat *London Edinburgh Dublin Phil. Mag. J. Sci.* **14** 108–27

[29] Maxwell J C II. 1860 Illustrations of the dynamical theory of gases *London Edinburgh Dublin Phil. Mag. J. Sci.* **20** 21–37

[30] Boltzmann L 2022 *Lectures on Gas Theory* (University of California Press)

[31] Eringen A C 2007 *Nonlocal Continuum Field Theories* (Springer)

[32] Eringen A C 1980 *Mechanics of continua R. E. Krieger Pub. Co*
[33] Irving J and Kirkwood J G 1950 The statistical mechanical theory of transport processes. IV. The equations of hydrodynamics *J. Chem. Phys.* **18** 817–29
[34] Chen Y 2009 Reformulation of microscopic balance equations for multiscale materials modeling *J. Chem. Phys.* **130** 134706
[35] Chen Y and Lee J 2005 Atomistic formulation of a multiscale field theory for nano/micro solids *Phil. Mag.* **85** 4095–126
[36] Chen Y, Shabanov S and McDowell D L 2019 Concurrent atomistic-continuum modeling of crystalline materials *J. Appl. Phys.* **126** 101101
[37] Chen Y 2024 Unifying temperature definition in atomistic and field representations of conservation laws *Proc. R. Soc.* A **480** 20230606
[38] Diaz A, Gu B, Li Y, Plimpton S J, McDowell D L and Chen Y 2022 A parallel algorithm for the concurrent atomistic-continuum methodology *J. Comput. Phys.* **463** 111140
[39] Xu S, Che R, Xiong L, Chen Y and McDowell D L 2015 A quasistatic implementation of the concurrent atomistic-continuum method for FCC crystals *Int. J. Plast.* **72** 91–126
[40] Chen H, Xu S, Li W, Ji R, Phan T and Xiong L 2018 A spatial decomposition parallel algorithm for a concurrent atomistic-continuum simulator and its preliminary applications *Comput. Mater. Sci.* **144** 1–10
[41] Deng Q, Xiong L and Chen Y 2010 Coarse-graining atomistic dynamics of brittle fracture by finite element method *Int. J. Plast.* **26** 1402–14
[42] Deng Q and Chen Y 2013 A coarse-grained atomistic method for 3D dynamic fracture simulation *J. Multiscale Comput. Eng.* **11** 227–37
[43] Xiong L and Chen Y 2009 Coarse-grained simulations of single-crystal silicon *Modelling Simul. Mater. Sci. Eng.* **17** 035002
[44] Xiong L, Deng Q, Tucker G J, McDowell D L and Chen Y 2012 Coarse-grained atomistic simulations of dislocations in Al, Ni and Cu crystals *Int. J. Plast.* **38** 86–101
[45] Xiong L, McDowell D L and Chen Y 2012 Nucleation and growth of dislocation loops in Cu, Al and Si by a concurrent atomistic-continuum method *Scr. Mater.* **67** 633–6
[46] Xu S, Xiong L, Chen Y and McDowell D L 2016 Edge dislocations bowing out from a row of collinear obstacles in Al *Scr. Mater.* **123** 135–9
[47] Xu S, Xiong L, Chen Y and McDowell D L 2016 An analysis of key characteristics of the Frank-Read source process in FCC metals *J. Mech. Phys. Solids* **96** 460–76
[48] Li Y, Gu B, Diaz A, Phillpot S R, McDowell D L and Chen Y 2023 Dislocation formation in the heteroepitaxial growth of PbSe/PbTe systems *Acta Mater.* **260** 119308
[49] Chen X, Xiong L, McDowell D L and Chen Y 2017 Effects of phonons on mobility of dislocations and dislocation arrays *Scr. Mater.* **137** 22–26
[50] Xiong L, McDowell D L and Chen Y 2014 Sub-THz Phonon drag on dislocations by coarse-grained atomistic simulations *Int. J. Plast.* **55** 268–78
[51] Li Y, Zheng Z, Diaz A, Phillpot S R, McDowell D L and Chen Y 2022 Resonant interaction between phonons and PbTe/PbSe (001) misfit dislocation networks *Acta Mater.* **237** 118143
[52] Chen X, Li W, Xiong L, Li Y, Yang S, Zheng Z, McDowell D L and Chen Y 2017 Ballistic-diffusive phonon heat transport across grain boundaries *Acta Mater.* **136** 355–65
[53] Li Y, Diaz A, Chen X, McDowell D L and Chen Y 2022 Interference, scattering, and transmission of acoustic phonons in Si phononic crystals *Acta Mater.* **224** 117481
[54] Chen Y and Lee J D 2003 Connecting molecular dynamics to micromorphic theory.(I). Instantaneous and averaged mechanical variables *Physica* A **322** 359–76
[55] Chen Y and Lee J D 2003 Connecting molecular dynamics to micromorphic theory.(II). Balance laws *Physica* A **322** 377–92
[56] Eringen A C 2012 *Microcontinuum Field Theories: I. Foundations and Solids* (Springer)
[57] Forest S 2016 Nonlinear regularization operators as derived from the micromorphic approach to gradient elasticity, viscoplasticity and damage *Proc. R. Soc.* A **472** 20150755
[58] Forest S 2013 Micromorphic Media *Generalized Continua from the Theory to Engineering Applications* (Springer) pp 249–300
[59] Bringen A C 1970 Balance laws of micromorphic mechanics *Int. J. Eng. Sci.* **8** 819–28
[60] Eringen A C 1964 Mechanics of micromorphic materials *Applied Mechanics: Proc. leventh Int. Congress of Applied Mechanics Munich* vol 1966 (Springer) pp 131–8
[61] Chen Y, Lee J and Eskandarian A 2003 Atomistic counterpart of micromorphic theory *Acta Mech.* **161** 81–102

[62] Dirac P 1930 *Principles of Quantum Mechanics*

[63] Schwartz L 1950 *Théorie des distributions* (Paris)

[64] Vladimirov V S, Jeffrey A and Schroeck F E 1971 Equations of mathematical physics *Am. J. Phys.* **39** 1548

[65] Diaz A, Davydov D and Chen Y 2019 On the equivalence of the two foundational formulations for atomistic flux in inhomogeneous transport processes *Proc. R. Soc.* A **475** 20180688

[66] Chen Y and Diaz A 2016 Local momentum and heat fluxes in transient transport processes and inhomogeneous systems *Phys. Rev.* E **94** 053309

[67] Chen Y and Diaz A 2018 Physical foundation and consistent formulation of atomic-level fluxes in transport processes *Phys. Rev.* E **98** 052113

[68] Chen Y 2016 The origin of the distinction between microscopic formulas for stress and Cauchy stress *EPL Europhys. Lett.* **116** 34003

[69] Rigelesaiyin J, Diaz A, Li W, Xiong L and Chen Y 2018 Asymmetry of the atomic-level stress tensor in homogeneous and inhomogeneous materials *Proc. R. Soc.* A **474** 20180155

[70] Cortés E, West B J and Lindenberg K 1985 On the generalized Langevin equation: classical and quantum mechanicala *J. Chem. Phys.* **82** 2708–17

[71] Tuckerman M 2023 *Statistical Mechanics: Theory and Molecular Simulation* (Oxford University Press)

[72] Chen X, Diaz A, Xiong L, McDowell D L and Chen Y 2018 Passing waves from atomistic to continuum *J. Comput. Phys.* **354** 393–402

[73] Dove M T 1993 *Introduction to Lattice Dynamics* (Cambridge University Press)

[74] Proville L, Rodney D and Marinica MC 2012 Quantum effect on thermally activated glide of dislocations *Nat. Mater.* **11** 845–9

[75] Stillinger F H and Weber T A 1985 Computer simulation of local order in condensed phases of silicon *Phys. Rev.* B **31** 5262–71

[76] Fan Z, Koster R S, Wang S, Fang C, Yalcin A O, Tichelaar F D, Zandbergen H W, Van Huis M A and Vlugt T J 2014 A transferable force field for CdS-CdSe-PbS-PbSe solid systems *J. Chem. Phys.* **141** 24

[77] Li Y, Fan Z, Li W, McDowell D L and Chen Y 2019 A multiscale study of misfit dislocations in PbTe/PbSe (001) heteroepitaxy *J. Mater. Res.* **34** 2306–14

[78] Pohl U W 2020 *Epitaxy of Semiconductors: Physics and Fabrication of Heterostructures* (Springer)

[79] Speck J, Brewer M, Beltz G, Romanov A and Pompe W 1996 Scaling laws for the reduction of threading dislocation densities in homogeneous buffer layers *J. Appl. Phys.* **80** 3808–16

[80] Romanov A, Pompe W, Beltz G and Speck J 1996 Modeling of threading dislocation density reduction in heteroepitaxial layers I. Geometry and crystallography *Phys. Status Solidi* b **198** 599–613

[81] Kasper E, Herzog H J and Kibbel H 1975 A one-dimensional SiGe superlattice grown by UHV epitaxy *Appl. Phys.* **8** 199–205

[82] Nakamura S 2015 Nobel Lecture: background story of the invention of efficient blue InGaN light emitting diodes *Rev. Mod. Phys.* **87** 1139

[83] Nakamura S, Mukai T, Senoh M S M and Iwasa N I N 1992 Thermal annealing effects on p-type Mg-doped GaN films *Jpn. J. Appl. Phys.* **31** L139

[84] Eaglesham D and Cerullo M 1990 Dislocation-free stranski-krastanow growth of Ge on Si (100) *Phys. Rev. Lett.* **64** 1943

[85] Narayan J and Sharan S 1991 Mechanism of formation of 60 and 90 misfit dislocations in semiconductor heterostructures *Mater. Sci. Eng.* B **10** 261–7

[86] Stukowski A and Albe K 2010 Extracting dislocations and non-dislocation crystal defects from atomistic simulation data *Mode.l Simul. Mat. Sci. Eng.* **18** 085001

[87] Springholz G and Wiesauer K 2001 Nanoscale dislocation patterning in PbTe/PbSe (001) lattice-mismatched heteroepitaxy *Phys. Rev. Lett.* **88** 015507

[88] McDowell D L 2024 Nonequilibrium statistical thermodynamics of thermally activated dislocation ensembles: part 3—Taylor–Quinney coefficient, size effects and generalized normality *J. Mater. Sci.* **59** 5161–200

[89] McDowell D L 2024 Nonequilibrium statistical thermodynamics of thermally activated dislocation ensembles: part 2—ensemble evolution toward correlation of enthalpy barriers *J. Mater. Sci.* **59** 5126–60

[90] McDowell D L 2024 Nonequilibrium statistical thermodynamics of thermally activated dislocation ensembles: part 1: subsystem reactions under constrained local equilibrium *J. Mater. Sci.* **59** 5093–125

[91] Chen G 2014 Multiscale simulation of phonon and electron thermal transport *Annu. Rev. Heat Transf* **17** 1–8

[92] Wilson R B and Cahill D G 2013 Anisotropic failure of Fourier theory in time-domain thermoreflectance experiments *Nat. Commun.* **5** 5075